Surface & Coatings Technology 452 (2023) 129125

Contents lists available at ScienceDirect

Surface & Coatings Technology

journal homepage: www.elsevier.com/locate/surfcoat

# Fabrication and growth mechanism of multilayered hydroxyapatite/organic composite coatings on the WE43 magnesium alloy

Juyi Yang [a,b], Yanbin Zhao [a,b], Jianwei Dai [a,b], Linyuan Han [a,b,*], Qiangsheng Dong [c], Lu Zhang [a,b], Jing Bai [a,b], Feng Xue [a,b], Paul K. Chu [d], Chenglin Chu [a,b,*]

[a] School of Materials Science and Engineering, Southeast University, Nanjing 211189, China
[b] Jiangsu Key Laboratory for Advanced Metallic Materials, Southeast University, Nanjing 211189, China
[c] School of Materials Science and Engineering, Jiangsu Key Laboratory of Advanced Structural Materials and Application Technology, Nanjing Institute of Technology, Nanjing 211167, China
[d] Department of Physics, Department of Materials Science and Engineering, Department of Biomedical Engineering, City University of Hong Kong, Hong Kong, China

ARTICLE INFO

*Keywords:*
Magnesium
Hydroxyapatite coating
Layer-by-layer assembly
Composite coating
Corrosion resistance

ABSTRACT

The design and fabrication of anti-corrosive coatings are important to medical implants, especially composite coatings consisting of soft organic and stiff inorganic materials with favorable mechanical properties and corrosion resistance. In this study, a polyethyleneimine/polyacrylic acid (PEI/PAA) multilayered coating is prepared by layer-by-layer (LbL) assembly on the WE43 Mg alloy, followed by mineralization of hydroxyapatite (HA) on the LbL multilayer. The composite coating with a compact surface shows improved corrosion resistance. The corrosion current density $i_{corr}$ decreases from 14.24 to 2.28 μA/cm$^2$ and the hydrogen emission rate diminishes from 0.0185 to 0.0105 mL·cm$^{-2}$·h$^{-1}$. The formation mechanism, structure, and properties of the organic/inorganic composite coating are investigated systematically. The LbL multilayer is found to play a significant role in initiating nucleation of HA and accommodate the lattice mismatch between the HA coating and WE43 substrate. This study enriches our understanding on the formation of organic/inorganic coatings and this type of composite coating has large potential in biomedical applications such as orthopedics.

## 1. Introduction

Orthopedic implants are frequently used in bone fixation, bone reconstruction, and fracture correction [1–3] and magnesium (Mg) and its alloys possessing natural biodegradability and elastic modulus more compatible with bones compared to stainless steels are desirable for these applications [4–7]. However, rapid hydrogen evolution and basification in the physiological environment must be addressed prior to clinical adoption. In this respect, surface modification [8–10] is a popular technique to enhance the corrosion resistance of Mg alloys. Calcium phosphate (Ca-P) coatings have attracted increasing interests for their excellent biocompatibility, corrosion resistance, and low cost [11–18]. However, the lattice mismatch between Ca-P coatings and magnesium alloys causes interfacial stress leading to accumulation of strain energy, formation of defects, low adhesion strength, and poor corrosion resistance. It is thus critical to optimize the mechanical properties, adhesion strength, corrosion resistance, durability, and degradation rate and understand the underlying mechanism.

Incorporating soft organic materials into anti-corrosion coatings is a good strategy and Ca-P coatings containing organic components have garnered attention. Biomimetic peptides containing negatively charged amino acids have been utilized to control Ca-P deposition on AZ31B and the coating exhibits a smooth and compact morphology in addition to better corrosion resistance [19]. Lin et al. [20] have prepared a polydopamine (PDA) - hydroxyapatite coating by immersion in the Ca-P solution for 48 h and PDA affects the morphology of calcium phosphate and improves the corrosion resistance of magnesium. Liu et al. [21] have used DNA with rich carboxyl groups to promote Ca-P formation in hydrothermal processes and the DNA/Ca-P coating has higher adhesion strength than the DNA-free one. In these cases, the organic constituents act as the nucleation initiator and crack arrester between the Ca-P coating and metal substrate.

To incorporate organic materials into anti-corrosion coatings, layer-by-layer (LbL) assembly is a promising method to control the components and thickness [22,23] and also to endow Mg alloys with self-healing, drug delivery, antibacterial properties [24,25]. Zhao et al.

* Corresponding authors at: School of Materials Science and Engineering, Southeast University, Nanjing 211189, China.
*E-mail addresses:* 101013242@seu.edu.cn (L. Han), clchu@seu.edu.cn (C. Chu).

https://doi.org/10.1016/j.surfcoat.2022.129125
Received 7 October 2022; Received in revised form 25 November 2022; Accepted 28 November 2022
Available online 7 December 2022

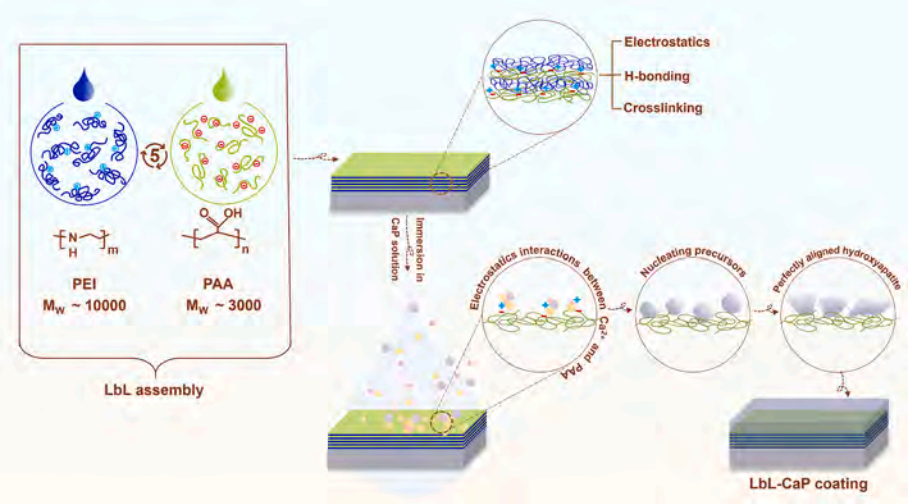


**Fig. 1.** Schematic diagram illustrating the fabrication process of the LbL-Ca-P coating.

**Table 1**
Concentration of the Ca-P solution.

| Concentration (mM) | | |
|---|---|---|
| $Ca(NO_3)_2{\cdot}4H_2O$ | $NaH_2PO_4{\cdot}2H_2O$ | $NaHCO_3$ |
| 14 mM | 8.4 mM | 4 mM |

**Table 2**
Concentration of the regeants in Hank's solution.

| Regeants | Concentration (g/L) |
|---|---|
| NaCl | 8 |
| KCl | 0.4 |
| $NaHCO_3$ | 0.35 |
| $MgSO_4{\cdot}7H_2O$ | 0.2 |
| $MgCl_2{\cdot}6H_2O$ | 0.1 |
| $CaCl_2$ | 0.14 |
| $Na_2HPO_4{\cdot}2H_2O$ | 0.06 |
| $KH_2PO_4$ | 0.06 |
| Glucose | 1 |

[26] have fabricated uniform and dense polyvinylpyrrolidone (PVP) and polyacrylic acid (PAA) multilayered coatings on Mg with excellent corrosion resistance and adhesion strength by the spin-assisted LbL method. The LbL multilayer facilitates formation of calcium phosphate in charged polyelectrolytes. For example, Cui et al. [27] have prepared negatively charged PAA as the outer layer in the $(PVP/PAA)_5$ structure. PAA contains carboxyl (-COOH) groups which interact with $Ca^{2+}$ to provide homogeneous nucleation sites for crystallization. Compared with the AZ31 Mg alloy, the WE43 alloy with an Al-free composition has better corrosion resistance and biocompatibility [28–30]. In this study, an organic/inorganic composite coating is prepared on the WE43 alloy and the influence of negatively charged PAA on crystallization of hydroxyapatite is investigated. The formation mechanism, structure, and properties are studied systematically.

## 2. Experimental details

### 2.1. Materials and methods

The commercially available WE43 alloy was cut into specimens with dimensions of 20 × 20 × 5 mm. Polyacrylic acid (PAA; $M_W$ ~ 3000 Da; 30 wt%) and polyethyleneimine (PEI; $M_W$ ~ 10,000 Da; 99 wt%) were purchased from Shanghai Macklin Biochemical Co., Ltd. Sodium hydroxide (NaOH) and sodium dihydrogen phosphate ($NaH_2PO_4{\cdot}2H_2O$) were obtained from Xilong Science Co., Ltd. and sodium bicarbonate ($NaHCO_3$) and calcium nitrate tetrahydrate ($Ca(NO_3)_2{\cdot}4H_2O$) were purchased from Sinopharm Chemical Reagent Co., Ltd. All the chemicals

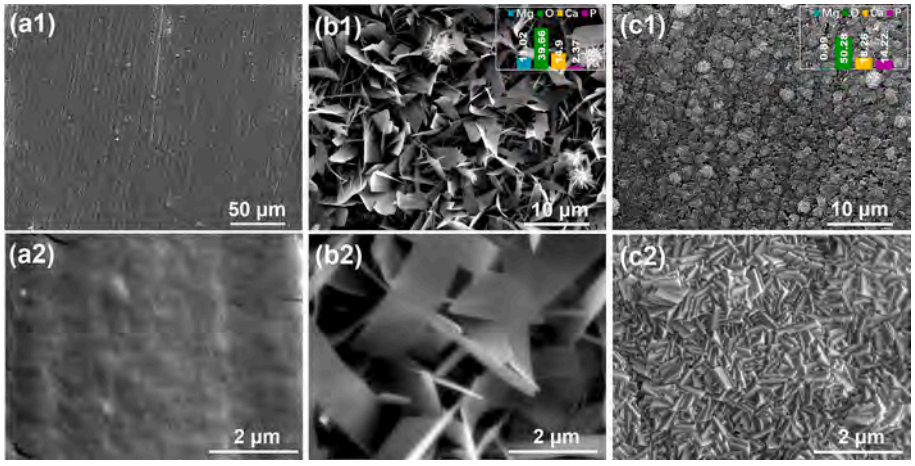


**Fig. 2.** SEM images of the coated samples: (a1, a2) LbL film, (b1, b2) Flaky structure of the Ca-P coating, and (c1, c2) Compact and integrated surface on the LbL-Ca-P coating.

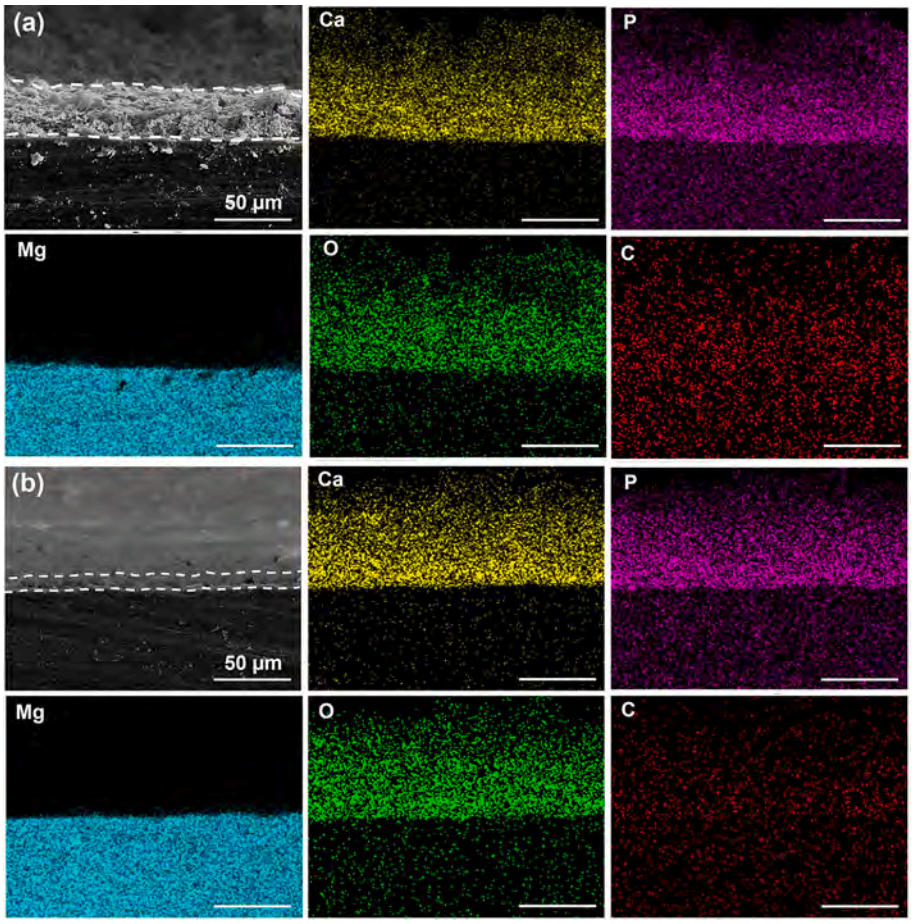


**Fig. 3.** Cross sectional images: (a) Ca-P coated sample and (b) LbL-Ca-P coated sample together with the EDS maps.

were used without purification. Deionized (DI) water was obtained by a Milli-Q system. Before coating preparation, the samples were ground with SiC paper progressively up to 2000 grids, rinsed with DI water and ethanol, and then dried in warm air. The substrates were immersed in 5.0 M NaOH for 20 min to provide the initial negative layer for subsequent LbL deposition. After the alkalization treatment, the samples were rinsed with DI water and dried at room temperature.

### 2.2. Fabrication of the LbL coating

The fabrication processes is shown schematically in Fig. 1. PEI (10 mg/mL) as the cationic polymer was dissolved in 18.2 MΩ deionized water. PAA (10 mg/mL) was the anionic polymer and the pH of PAA was adjusted to 7.0 by adding 1.0 M sodium hydroxide (NaOH). The hydroxylated samples were dipped in the PEI solution for 5 min and rinsed with DI water. The intermediate drying step was critical to the film uniformity and compactness. The positively charged samples were immersed in the PAA solution for another 5 min, rinsed, and dried. The cycle was repeated five times to fabricate the $(PEI/PAA)_5$ multilayered film on the WE43 substrate (denoted as LbL). The LbL coated samples were dried at 110 °C for 45 min.

### 2.3. Fabrication of the LbL-Ca-P coating

$Ca(NO_3)_2{\cdot}4H_2O$ and $NaH_2PO_4{\cdot}2H_2O$ were dissolved separately in 50 mL DI water and $NaHCO_3$ was added to the phosphate solution as a nucleating agent. The final concentration of the solution is listed in Table 1 [23] and the Ca/P ratio was 1.67. The $NaH_2PO_4{\cdot}2H_2O$ solution was added to the $Ca(NO_3)_2{\cdot}4H_2O$ solution dropwise to produce a metastable state and the supersaturated solution remained transparent [17]. The samples with and without the LbL coating and Ca-P solution were transferred to an autoclave and hydrothermally treated at 90 °C for 4 h [28]. Afterwards, the Ca-P-coated samples were removed, rinsed with DI water, and dried at 70 °C (denoted as Ca-P and LbL-Ca-P).

### 2.4. Surface characterization

The surface morphology of the LbL, Ca-P, and LbL-Ca-P coatings was examined on the Sirion field-emission scanning electron microscope (SEM) at 20 kV. The composition of the coatings was determined by energy-dispersive X-ray spectroscopy (EDS). XRD was carried out to determine the structure of the Ca-P coatings using a Cu-$K_\alpha$ X-ray source (1.5418 Å) and Ψ (tilt angle) was increased from 10 to 90 in steps of 10°/min. Fourier transform infrared spectroscopy (FTIR) was performed on the Nicolet iS10 (USA) in the range of 500 to 4000 $cm^{-1}$ with a resolution of 0.4 $cm^{-1}$.

### 2.5. In vitro degradation assessment

#### 2.5.1. Electrochemical measurements

The electrochemical properties were determined using the Princeton electrochemical workstation (Ametek PARSTAT 3000A-DX) with a three-electrode configuration. The sample with an exposed area of 1 $cm^2$ was the working electrode, whereas the saturated calomel electrode and Pt sheet were the reference and counter electrodes, respectively. Electrochemical impedance spectroscopy (EIS) was conducted with an AC amplitude of 10 mV AC between 100 kHz and 100 mHz and potentiodynamic polarization was performed at a scanning rate of 1 mV/s with the potential (vs SCE) from −2.5 V to −1 V. The process was carried out in Hank's solution (Table 2) at 37.5 ± 0.1 °C. The bare WE43 sample was

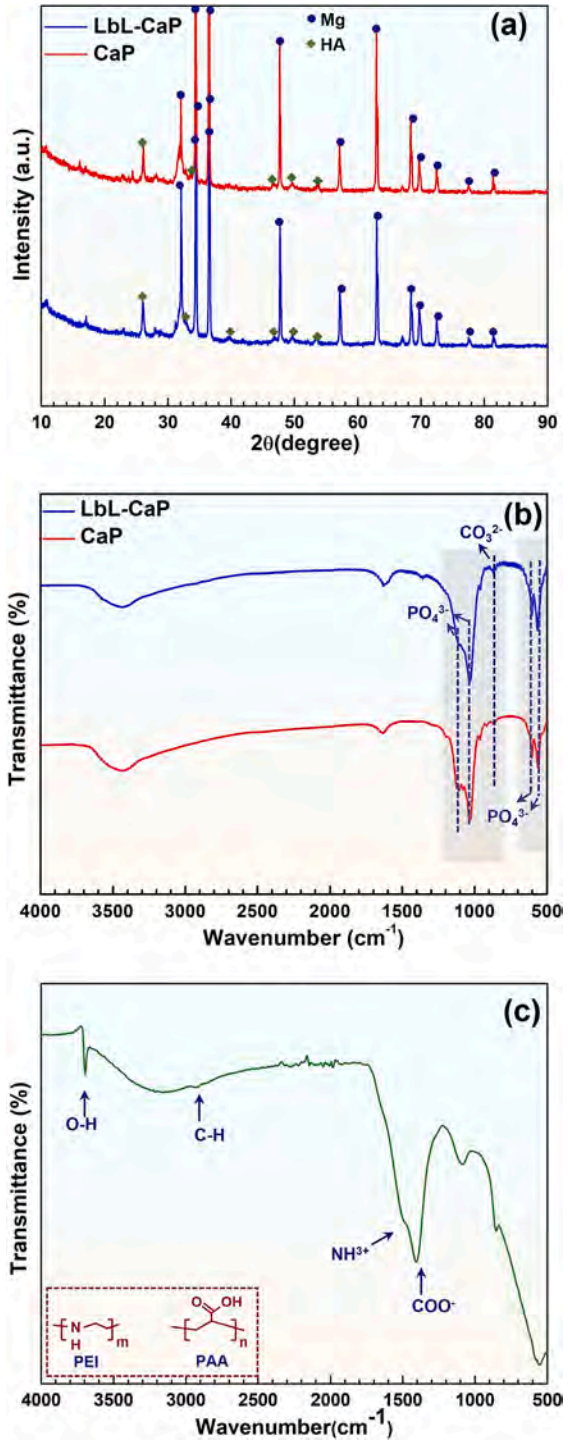


**Fig. 4.** (a) XRD patterns and (b) FTIR spectra of the Ca-P and LbL-Ca-P coatings; (c) FTIR spectrum of the LbL coating.

the control and the data were analyzed by the Versastudio and ZSimpWin software.

#### 2.5.2. Hydrogen evolution

The samples were immersed in Hank's solution for 100 h at 37.5 ± 0.1 °C to measure $H_2$ evolution. Each sample was placed under a funnel filled with Hank's solution and the space between the funnel and beaker was hermetic. The burette above the funnel collected the emitted hydrogen [31] and three tests were performed to improve the statistics. The hydrogen evolution rate (HER) is defined as [27]:

$$v_H = V/(st) \quad (1)$$

where $V$ is the volume of hydrogen emitted, and $s$ and $t$ are surface area and immersion time, respectively. After the test, the samples were removed from Hank's solution, rinsed with DI water, and then dried with warm air.

### 2.6. Mechanical properties

The adhesion strength was measured using the Nano Test system equipped with a diamond indenter tip (120° peak angle, tip radius $R$ = 0.2 mm). A scratch track with a length of 2 mm length was formed when the load was raised gradually from 0 to 20 N at a rate of 1 mm/min. Three separate tracks were made on each coating and the distance between each track was larger than 3 mm. The scratches were observed under an optical microscope and the images were recorded. The hardness (H) and elastic modulus (E) of the Ca-P and LbL-Ca-P coatings were determined on the Nano Test System (Micro Materials) using a Berkovich indenter tip at a maximum load of 550 μN.

## 3. Results

### 3.1. Coating characterization

To improve the corrosion resistance and biocompatibility of the WE43 Mg alloy and facilitate mineralization of the hydroxyapatite (HA) coating, the PEI/PAA multilayer is prepared by the LbL method. Fig. 2 (a1, a2) shows that the LbL coating is uniform and smooth. Fig. 2(b1, b2) reveals the loose structure in the Ca-P layer with randomly oriented flaky crystals with the preferential orientation along the c-axis. The LbL-Ca-P coating (Fig. 2(c1, c2)) shows a tightly packed structure comprising lamellar-like crystals approximately 600–800 nm in length. The cross-sectional images in Fig. 3 show that the pure Ca-P layer is thicker than the induced-Ca-P layer because of the influence of the LbL multilayer on nucleation of calcium phosphate. The Ca/P atomic ratios of the Ca-P and induced-Ca-P coatings are 1.28 and 1.16, respectively. SEM discloses a compact and dense induced-Ca-P layer as a result of the optimized interface state and nucleation by the negatively charged carboxyl groups in the PAA chains [27].

The XRD and FTIR spectra are displayed in Fig. 4. The Ca-P and LbL-Ca-P coatings show the hydroxyapatite phase with high crystallinity. The peaks of Ca-P and LbL-Ca-P at 26.15°, 46.9°, 49.8°, and 59.7° stem from the (002), (222), (213), and (004) planes of hydroxyapatite [17,28]. FTIR confirms formation of the Ca-P phase. The spectra of the two Ca-P coatings show bands at 600–1115 $cm^{-1}$ associated with $PO_4^{3-}$ and the peak at 871 $cm^{-1}$ indicates carbonate involved in the crystallization of HA. For LbL coating shown in Fig. 4(c) has COOH in PAA as indicated by the peak at 1408 $cm^{-1}$ and the peak at 1499 $cm^{-1}$ is associated with -N-H in PEI, thereby corroborating fabrication of the LbL film on the WE43 substrate [32,33].

The scratch test is performed to obtain the critical rupture load and measure the adhesion strength of different coatings. Fig. 5 shows that the Ca-P and LbL-Ca-P coatings reach the critical loads of 2.46 and 3.98 N, respectively, confirming that the LbL-Ca-P coating adheres more tightly to the WE43 substrate, possibly because the LbL multilayer buffers the lattice mismatch between hydroxyapatite and the substrate. The buffering effect will be discussed in details later. The hardness (H) and elastic modulus (E) calculated from the load−depth curves (Fig. 5) are listed in Table 2. The $H$ and $E$ values of the Ca-P and LbL-Ca-P coatings are 7.10 ± 0.03, 12.80 ± 0.03 MPa and 0.46 ± 0.04, 0.81 ± 0.11 GPa respectively. They are less than those of the hydroxyapatite coating reported by Yılmaz et al. [34], probably because that the indenter pressure did not act directly on the substrate due to the rough surface.

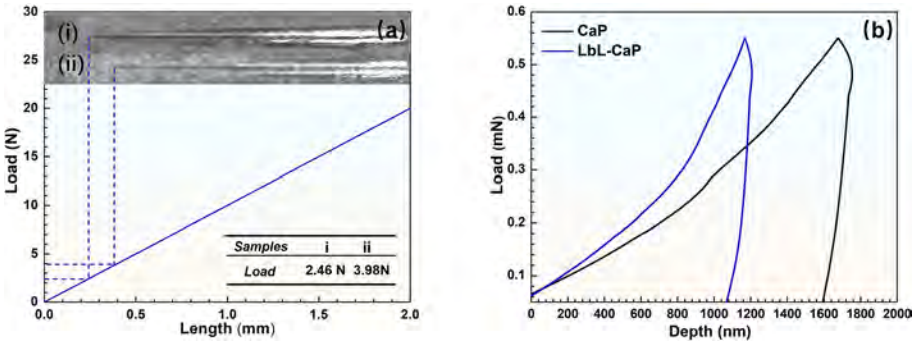


**Fig. 5.** (a) Scratch test results where (i) refers to the Ca-P coating and (ii) represents LbL-Ca-P coating; (b) Load−depth curves obtained by nanoindentation.

**Table 3**
Hardness (*H*) and elastic modulus (*E*) values of the Ca-P and LbL-Ca-P coatings.

| Samples | Hardness (H, MPa) | Elastic Modulus (E, GPa) |
|---|---|---|
| Ca-P | 7.1 ± 0.034 | 0.46 ± 0.041 |
| LbL-Ca-P | 12.8 ± 0.028 | 0.81 ± 0.11 |

### 3.2. In vitro degradation

Corrosion of magnesium in an aqueous solution occurs as follows:

$$Mg + 2H_2O \rightarrow Mg^{2+} + 2OH^- + H_2 \quad (2)$$

Electrochemical methods such as potentiodynamic polarization (PDP) and electrochemical impedance spectroscopy (EIS) can be used to assess the corrosion behavior such as the corrosion mechanism, corrosion tendency, and corrosion resistance of difference coatings. The potentiodynamic polarization curves are displayed in Fig. 6 and $E_{corr}$ (corrosion potential) and $i_{corr}$ (corrosion current density) calculated by extrapolation are listed in Table 3. Compared with the bare WE43 substrate, the corrosion current densities of the LbL-Ca-P and Ca-P coated specimens decrease remarkably from 14.24 to 5.10 and 2.28 μA/cm$^2$, respectively, indicating significant improvement after surface modification. However, $i_{corr}$ is similar for the LbL-Ca-P and Ca-P coatings. The latter is thicker than the former (Fig. 2) and a thicker film impedes penetration of the corrosive ions. Therefore, despite lacking in the density and compactness, the Ca-P coating is able to control degradation of the WE43 alloy.

$E_{corr}$ increases slightly after surface modification because of the compromised integrity of magnesium after the hydrothermal process. The rare-earth elements such as Gd, Y, and Nd help to produce a homogeneous microstructure to reduce corrosion. As a thermodynamic parameter, $E_{corr}$ can be used to evaluate the corrosion tendency, but is limited for measuring the corrosion resistance directly. The anodic polarization curve of the bare WE43 shows a steady increase of $i_{corr}$ and the same region for all the coated samples show relatively steep curves illustrating impeded polarization in the presence of the anti-corrosion coatings. The Nyquist plots show obvious difference in the radii of the capacitive reactance arcs between WE43 and the other coated samples. Specifically, the radii follow the order of LbL-Ca-P > Ca-P > WE43, revealing enhanced corrosion resistance. The equivalent electrical circuit (EEC) are shown in Fig. 6 (j) and the fitting parameters are listed in Table 4, in which $R_s$, $R_{ct}$, and $R_f$ are the solution resistance, charge transfer resistance, and coating resistance, respectively. The polarization resistance representing polarization difficulty exhibits the following order of LbL-Ca-P (2.22E4 ohm) > Ca-P (1.15E4 ohm) > WE43 (3.32E3 ohm).

Electrochemical tests are carried out after immersion in Hank's solution for 7 days to monitor the corrosion resistance. The potentiodynamic curves and EIS results are displayed in Fig. 6 and Tables 4 and 5. Corrosion of the bare Mg matrix in Hank's solution leads to the formation of a 10 μm thick layer on the surface (Fig. 10) which subsequently contributes to the increase in the capacitive arc radius and $|Z|_{0.1Hz}$ value. $i_{corr}$ and $R_p$ of the LbL-Ca-P coated sample are 3.52 μA and 1.9E4 ohm, respectively. It can be inferred that the LbL-Ca-P coating provides an excellent anti-corrosion barrier during immersion in Hank's solution. In conclusion, PDP and EIS suggest that the LbL-Ca-P treatment is effective in controlling degradation of the WE43 substrate.

Compared to electrochemical methods, immersion tests are used to evaluate the degradation properties over a long period of time. Hence, this technique is generally carried out in conjunction with electrochemical methods to characterize the corrosion resistance of biomaterials. Fig. 7 presents the hydrogen evolution profiles of WE43, LbL, Ca-P, and LbL-Ca-P during immersion for 100 h. Generally, the hydrogen evolution rate (HER) shows the following order of LbL-Ca-P < Ca-P < LbL < WE43, revealing that the LbL-Ca-P coating has excellent corrosion resistance but the pure LbL layer provides only limited resistance on account of the loose structure. $H_2$ evolution exhibits a roughly linear trend in the first 3 h (enlarged profiles in Fig. 7 (a)) and then declines gradually before reaching a steady state after 50 h. The WE43 substrate shows the biggest hydrogen evolution rate of 0.0185 mL·cm$^{-2}$·h$^{-1}$ and the LbL-Ca-P sample shows the smallest lowest rate of 0.0105 mL·cm$^{-2}$·h$^{-1}$. In general, the immersion data are consistent with the electrochemical results thus confirming the advantages rendered by the LbL multilayer.

The XRD and FTIR spectra acquired after immersion are presented in Fig. 7. Immersion accelerates degradation but also provides calcium and phosphate for mineralization. Consequently, mineralization produces new features in the FTIR spectra (Fig. 7(c)). For example, WE43 and LbL-WE43 show bands $\nu_3$ (950–1150 cm$^{-1}$) and $\nu_4$ (450–650 cm$^{-1}$) of phosphate after immersion, but the XRD patterns do not show distinct peaks from calcium phosphate suggesting that the mineral component is amorphous. Furthermore, owing to the stable chemical structure of HA, the XRD patterns and FTIR spectra of the Ca-P and LbL-Ca-P coated samples do not change significantly.

Fig. 8 compares the macroscopic morphology of the samples after immersion for 7 days. The Ca-P and LbL-Ca-P coated samples show minor changes, but the LbL coated and uncoated samples transition to a rustic brown color due to corrosion. The uncoated Mg substrate shows visible corroded holes with a diameter of about 2–3 mm. The SEM images in Fig. 9(a-d) reveal clear differences in the corroded morphologies of the four samples. Both WE43 and LbL-WE43 show grid-like cracks after immersion but Fig. 9(b2) shows that the LbL coated sample has shallower cracks compared to Fig. 9(a2) due to less hydrogen evolution shown in Fig. 7(a). The undulating surface of the LbL coating indicates that the multilayer does not disintegrate completely in the immersion test. EDS discloses that the corrosion products on these two samples are composed of magnesium and calcium phosphate. In addition, the Ca-P coated sample shows several microcracks as shown in Fig. 9(c1, c2), but the LbL-Ca-P coating remains almost intact and the minor

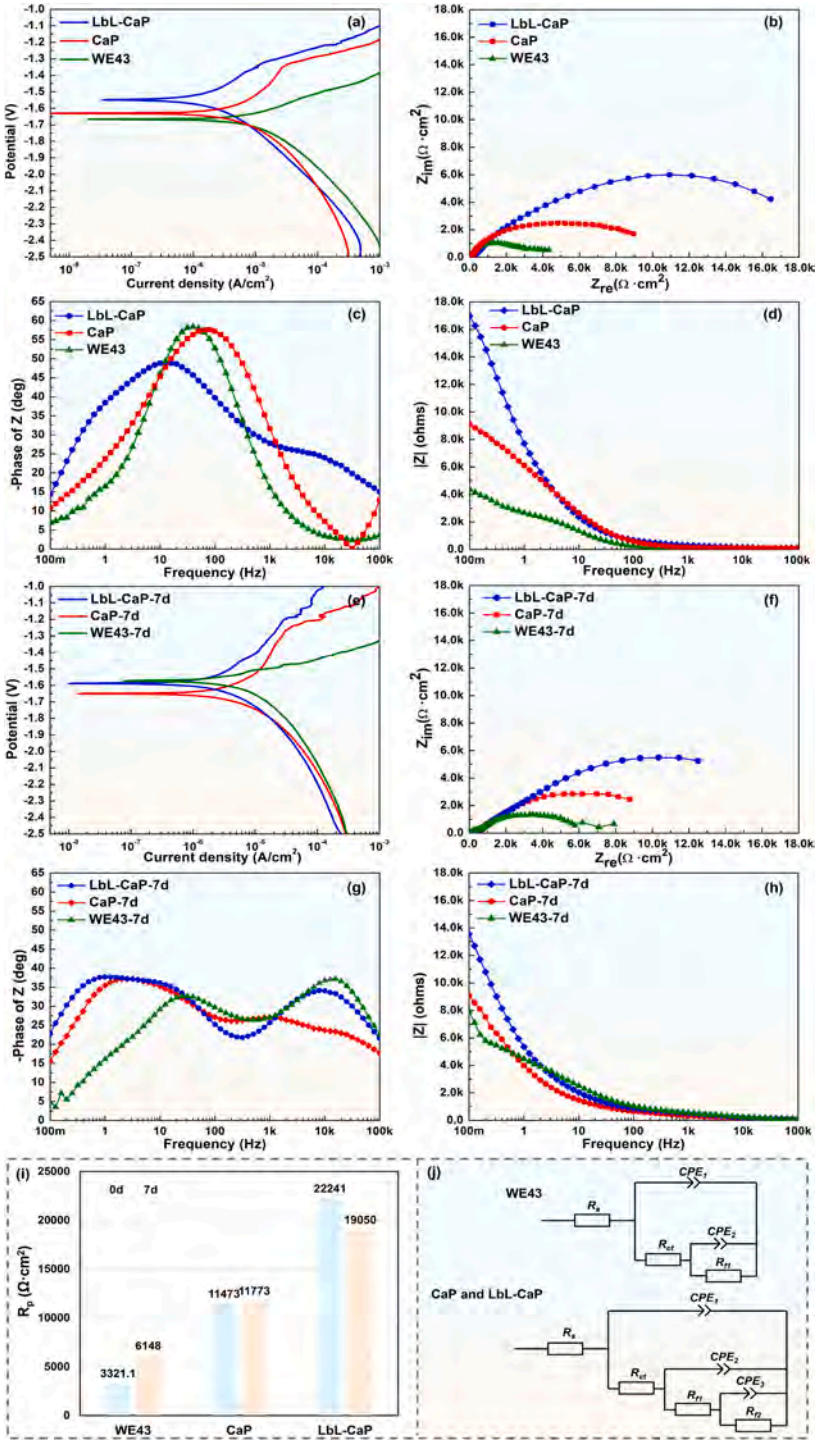


**Fig. 6.** Electrochemical measurements of the bare WE43 substrate, Ca-P, and LbL-Ca-P coated samples in Hank's solution for 0 and 7 days: (a, e) Potentiodynamic polarization curves, (b, f) Impedance spectra, (c, d, g, h) Bode Plots, (i) Polarization resistance $R_p$, and (j) Equivalent circuits for the impedance spectra.

morphological change can be attributed to mineralization during immersion. The Ca/P ratio calculated from point d4 is 1.44 that is closer to the stoichiometric ratio of hydroxyapatite compared to the original value of 1.16. SEM shows that more cracks are generated and propagate if the $H_2$ emission rate is larger. According to the cross-sectional images in Fig. 10, the substrates with and without the anti-corrosion coatings maintain the bulk integrity after immersion because the cracks are confined to the surface region due to the good corrosion resistance of the WE43 substrate.

**Table 4**
$E_{corr}$ and $i_{corr}$ determined from the potentiodynamic polarization curves.

| Samples | $E_{corr}$ (V/SCE) | $i_{corr}$ (μA/cm²) |
|---|---|---|
| WE43 | −1.66 | 14.24 |
| Ca-P | −1.68 | 5.10 |
| LbL-Ca-P | −1.54 | 2.28 |
| WE43-7 d | −1.57 | 16.90 |
| Ca-P-7 d | −1.65 | 5.62 |
| LbL-Ca-P-7 d | −1.59 | 3.52 |

**Table 5**
Fitted EIS results from the Nyquist Plots.

| Samples | Rs ($\Omega \cdot cm^2$) | $CPE_1$ ($\Omega^{-1} \cdot s^n \cdot cm^{-2}$) | $n_1$ | $R_{f1}$ ($\Omega \cdot cm^2$) | $CPE_2$ ($\Omega^{-1} \cdot s^n \cdot cm^{-2}$) | $n_2$ | $R_{f2}$ ($\Omega \cdot cm^2$) | $CPE_3$ ($\Omega^{-1} \cdot s^n \cdot cm^{-2}$) | $n_3$ | $R_{ct}$ ($\Omega \cdot cm^2$) |
|---|---|---|---|---|---|---|---|---|---|---|
| WE43 | 96.25 | 1.52E-5 | 0.883 | 2479 | 3.53E-5 | 0.886 | – | – | – | 842.1 |
| Ca-P | 105.9 | 1.60E-6 | 0.966 | 86.56 | 1.00E-5 | 0.725 | 4706 | 1.02E-4 | 0.500 | 6681 |
| LbL-Ca-P | 71.13 | 1.47E-5 | 0.572 | 352.4 | 1.63E-5 | 0.660 | 3199 | 4.95E-7 | 0.985 | 1.869E4 |
| WE43-7d | 70.03 | 1.02E-6 | 0.754 | 494.1 | 3.19E-5 | 0.576 | – | – | – | 5654 |
| Ca-P-7d | 67.50 | 4.08E-6 | 0.640 | 175.9 | 1.41E-5 | 0.617 | 617.5 | 5.16E-5 | 0.624 | 1.098E4 |
| LbL-Ca-P-7d | 69.07 | 4.14E-6 | 0.640 | 758.9 | 2.02E-5 | 0.751 | 3992 | 4.69E-5 | 0.729 | 1.43E4 |

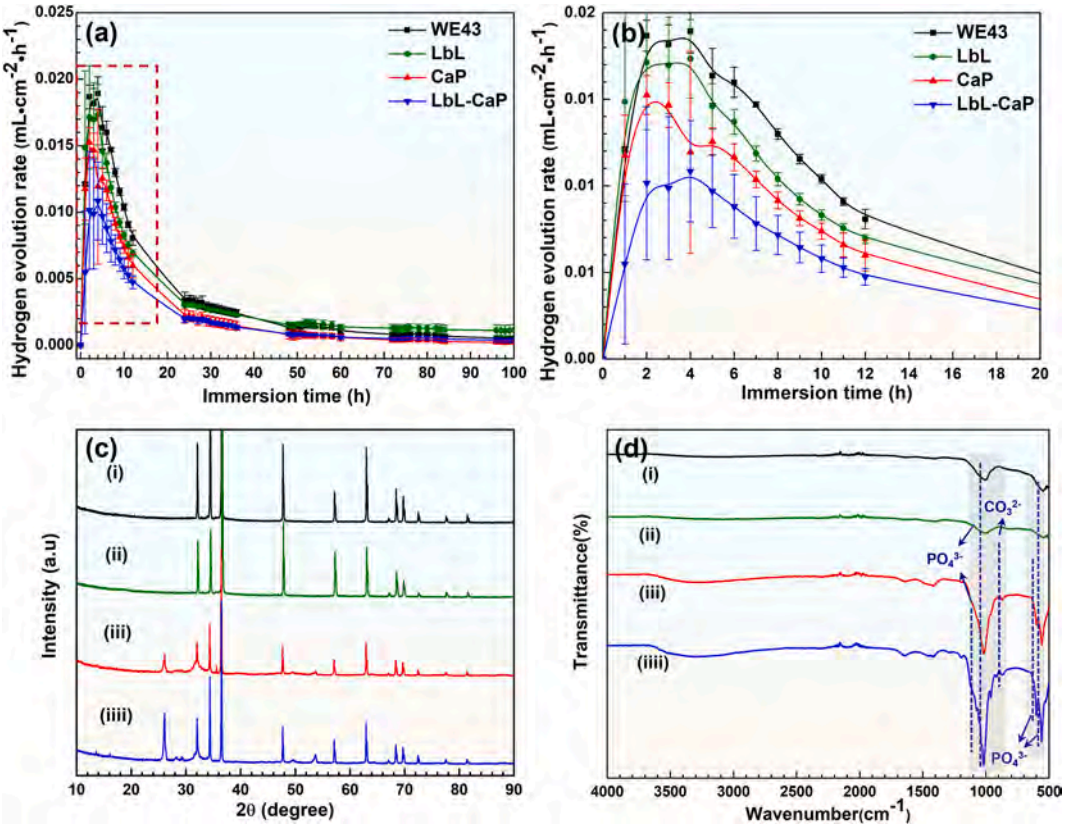


**Fig. 7.** (a) HER curves and (b) Enlarged curves in the red box in (a); (c) XRD patterns and (d) FTIR spectra after the immersion test: (i) WE43, (ii) LbL, (iii) Ca-P, and (iiii) LbL-Ca-P.

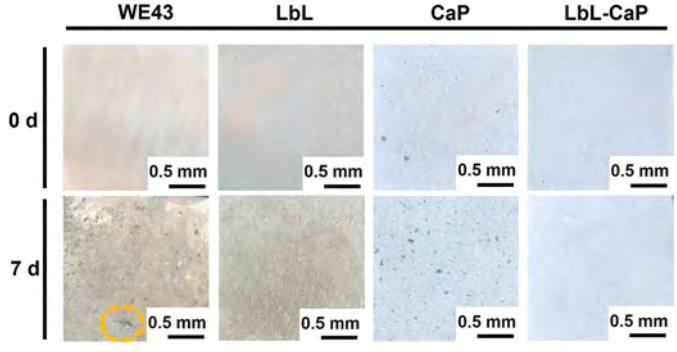


**Fig. 8.** Macroscopic morphology of the various samples after immersion for 7 days.

## 4. Discussion

### 4.1. Formation mechanism of the LbL-Ca-P coating

LbL is a versatile technique to prepare functional coatings and the properties depend on parameters such as the molecular weight, pH, and ionic strength [25,35]. In this work, a LbL multilayered Ca-P coating is fabricated on the WE43 alloy and the formation mechanism is described as follows. Initially, the alkali-treated substrate exposes a negatively charged hydrophilic surface to which the positively charged PEI chains are attracted electrostatically. Subsequent layer-by-layer assembly involves alternating deposition of PEI and PAA driven by complementary interactions. Furthermore, PAA is almost fully ionized at the pH of 7.0 and adopts an extended configuration in the solution, whereas PEI shows coil-like conformation with insufficient ionization at the pH of 11.0 [36]. Yang et al. [37] have suggested that the PEI and PAA chains in the LbL film are interpenetrating due to the electrostatic interaction,

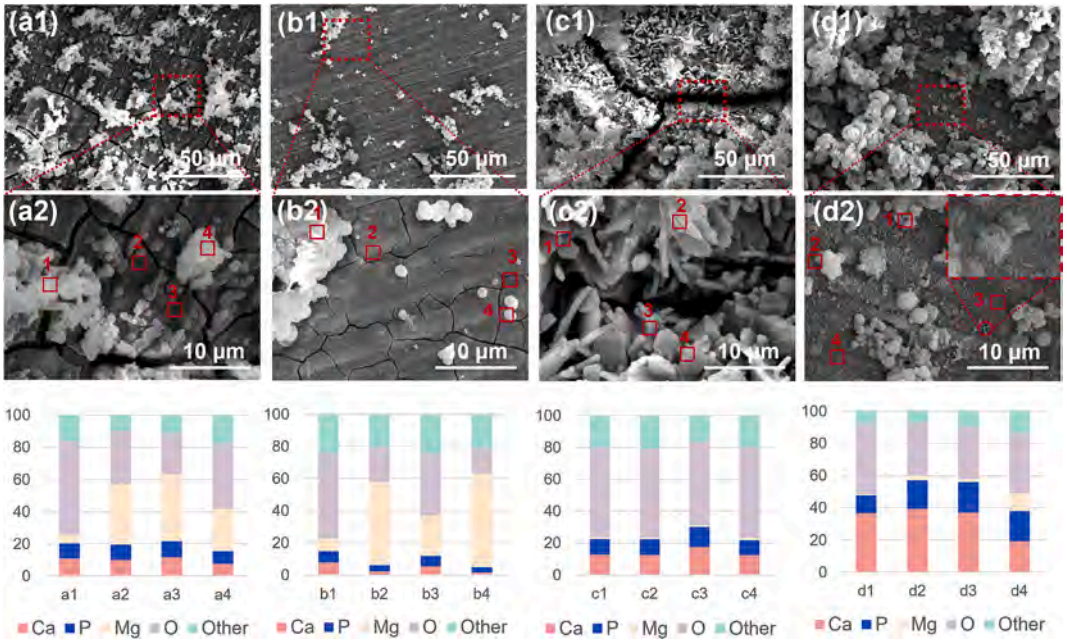


**Fig. 9.** (a1, a2), (b1, b2), (c1, c2), and (d1, d2) SEM images and EDS results (atomic ratio) of WE43, LbL, Ca-P, LbL-Ca-P immersed in Hank's solution for 7 d, respectively.

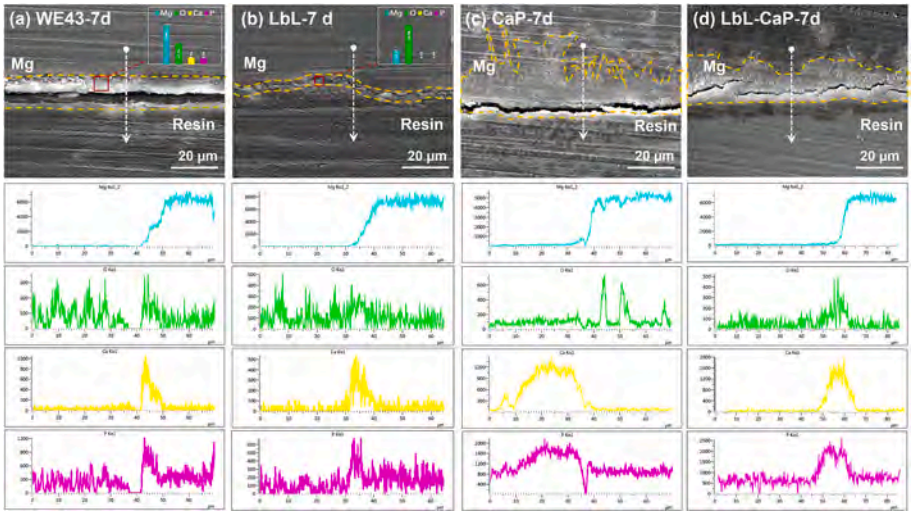


**Fig. 10.** Cross-sectional SEM images and EDS line scans: (a) WE43; (b), (c), and (d) LbL, Ca-P, and LbL-Ca-P coated WE43 samples after immersion for 7 days.

intermolecular hydrogen bonding, and cross-linking as shown in Fig. 1.

Subsequent mineralization proceeds via electrostatic interactions between PAA and $Ca^{2+}$. Specifically, the loosely aggregated pre-nucleation clusters (e. g. $Ca^{2+}$, $PO_4^{3-}$, $HPO_4^{2-}$, $OH^-$) are bound electrostatically to the negatively charged surface of PAA. The clusters aggregate near the surface to produce a high degree of supersaturation and form amorphous particles as nucleation precursors, leading to gradual crystallization and formation of ordered HA [38].

The LbL-Ca-P and Ca-P coatings show remarkable differences such as the morphology shown in Fig. 2 because PAA improves the interface state between HA and the substrate. The optimal interfacial conditions decrease the nucleation barrier and promote the formation of perfectly aligned hydroxyapatite crystals [39]. The nucleation barrier follows the following relationship [39]:

$$\Delta G^* = \Delta G^*_{homo} f(m)\ (0 \le f \le 1) \quad (3)$$

where $\Delta G^*_{homo}$ is the homogeneous nucleation barrier and $f(m)$ represents the interface correlation factor between 0 and 1. When $f(m) \to 0$, the optimal interfacial conditions are achieved and $\Delta G^*$will be lower than $\Delta G^*_{homo}$. According to Eq. (3), the electrostatic interactions between PAA and $Ca^{2+}$ suppress the interfacial mismatch and reduce $\Delta G^*$to promote heterogeneous nucleation with adequate sites. On the contrary, in the absence of the LbL multilayer, supersaturation-driven interfacial mismatch between the Ca-P coating and substrate and oriented-growth of rib-like crystals are observed. Meanwhile, the pH decreases from 6.4 to 5.6 after mineralization, indicating that the formation of hydroxyapatite consumes $OH^-$. The $CO_3^{2-}$ peak at 871 $cm^{-1}$ in Fig. 4 suggests that carbonate plays an important role in nucleation of HA.

### 4.2. Formation mechanism, structure, and properties

The contributions of the LbL multilayer are summarized in the

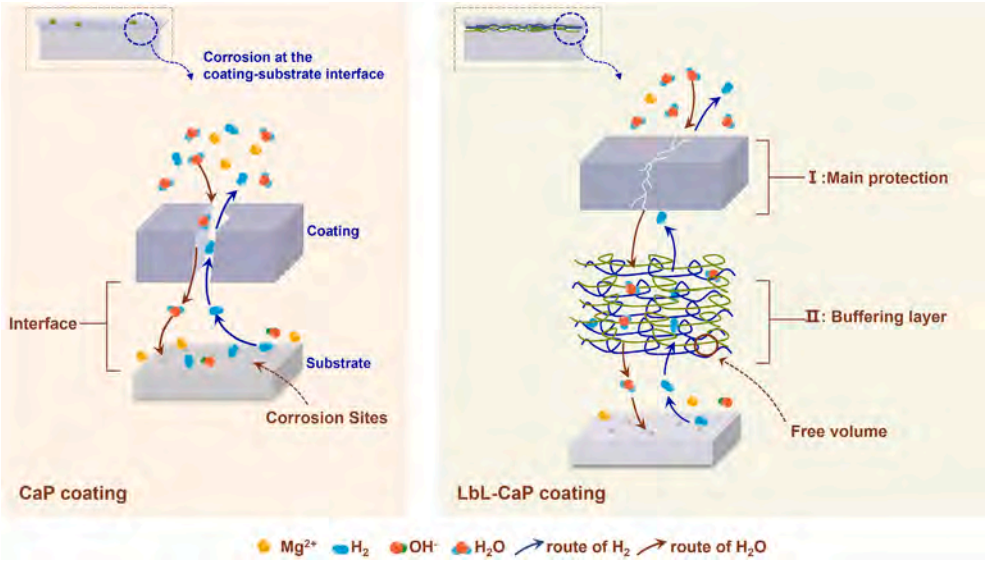


**Fig. 11.** Corrosion mechanism of WE43 with the Ca-P and LbL-Ca-P coatings.

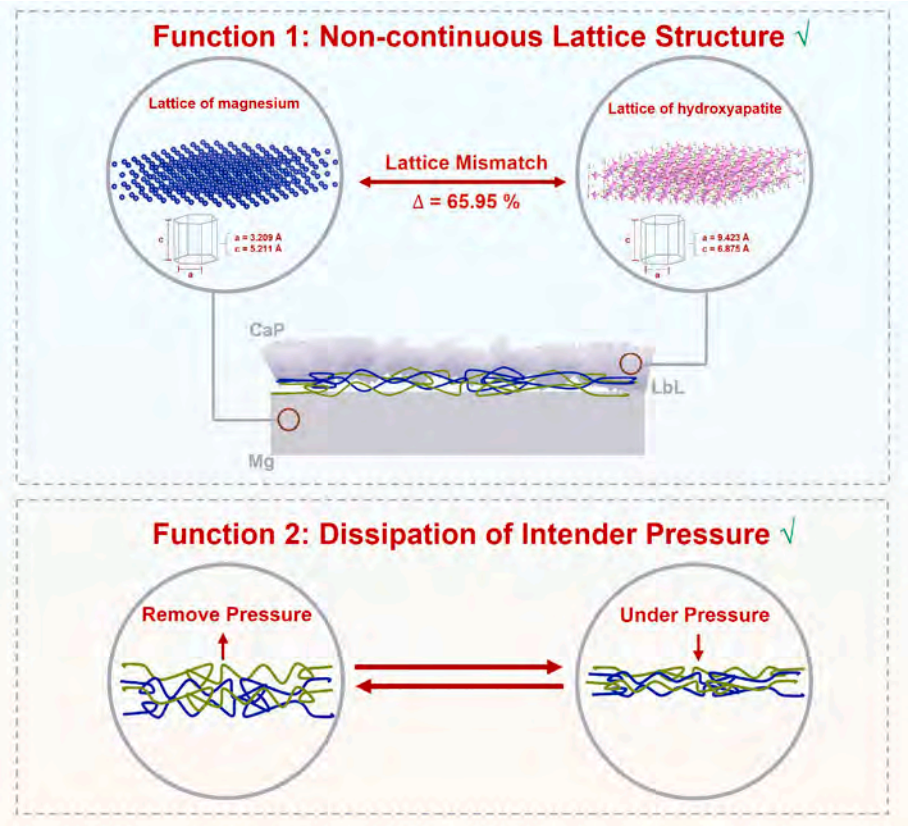


**Fig. 12.** Schematic diagrams illustrating enhanced adhesion strength of the LbL-Ca-P coating.

following. Firstly, the LbL multilayer initiates nucleation of tightly-arranged HA crystals [40]. The electrostatic interactions between PAA and $Ca^{2+}$ promote the formation of the compact and uniform coating with enhanced corrosive resistance and adhesion strength. Secondly, the multilayer helps the creation of a sandwiched structure by acting as a buffering layer between HA and the substrate.

The corrosion models for the LbL-Ca-P and Ca-P coatings are postulated in Fig. 11. According to Eq. (2), inward diffusion of water molecules and other aggressive anions through the loose Ca-P coating causes Mg degradation and $H_2$ emission [27]. Consequently, a local pressure is formed at the coating-substrate interface from hydrogen evolution lead to the formation and propagation of cracks through the Ca-P coating (Fig. 8). In contrast, the inorganic coating containing the LbL layer provides a dual protection barrier. The dense hydroxyapatite layer assumes the main role of anti-corrosion but the PAA/PEI multi-layer with a relative loose structure offers only weak protection. The LbL layer decrease the hydrogen evolution rate by providing the necessary volume [41–44] between polymer chains to trap and store $H_2$ molecules,

which in turn reduces the interfacial pressure. In this way, the integrity of the Ca-P coating is maintained during immersion resulting in long-term corrosion resistance as shown in Fig. 7.

The scratch test results shown in Fig. 5 demonstrate that the LbL-Ca-P coating has better adhesion strength which can be attributed to the synergy described in Fig. 12. Accumulation of strain energy resulting from lattice mismatch between Mg and HA can be effectively alleviated by the buffering polymer providing structural stability [45]. The lattice mismatch can be determined quantitatively as follows [46]:

$$\Delta = (a_{max} - a_0)/a_{max} \quad (4)$$

where Δ (%) represents the mismatch factor, $a_0$ (Å) is the interatomic distance, and $a_{max}$ (Å) is the maximum interatomic distance of the two lattice structures. Accordingly, there is high mismatch (65.95 %) in the lattice parameters between Mg (0001) and hydroxyapatite (0001). The polymer layer can accommodate this large lattice mismatch by discrete connection between the two different lattice structures [47]. Moreover, the free volume allows deformation and rearrangement of the polymer chains and partial dissipation of internal pressure when the samples are subjected to external forces [48,49]. As a result, the interfacial strength of the LbL-Ca-P coating is improved.

## 5. Conclusion

An organic/inorganic coating with the PEI/PAA multilayered structure as the nucleation initiator and crack arrester is prepared on the WE43 Mg alloy. Owing to the electrostatic interactions between negatively charged PAA and $Ca^{2+}$, the LbL-Ca-P coating has a compact and dense surface. The calcium phosphate coating and LbL multilayer serve as a dual-functional protection barrier to minimize degradation of the WE43 alloy and the adhesion strength improves due to the LbL layer as well. The buffering effects rendered by the LbL layer and subsequent effects on the degradation and interfacial mismatch are studied. The results provide insights into the design and fabrication of organic/inorganic coatings for biomedical applications and guidance in future research pertaining to clinical application of Mg alloys to orthopedics and other medical fields.

## CRediT authorship contribution statement

**Juyi Yang:** Conceptualization, Methodology, Fabrication, Writing - original draft, Writing - review & editing. **Yanbin Zhao:** Conceptualization, Methodology, Writing - review & editing. **Jianwei Dai:** Writing - review & editing. **Linyuan Han:** Supervision. **Qiangsheng Dong:** Writing - review & editing. **Lu Zhang:** Writing - review & editing. **Jing Bai:** Methodology. **Feng Xue:** Methodology. **Paul K. Chu:** Writing – review & editing. **Chenglin Chu:** Supervision, Methodology.

## Declaration of competing interest

The authors declare that they have no known competing financial interests or personal relationships that could have appeared to influence the work reported in this paper.

## Data availability

No data was used for the research described in the article.

## Acknowledgements

This research was supported by the National Natural Science Foundation of China (No. 52171236), Open Research Fund of Jiangsu Key Laboratory for Advanced Metallic Materials (No. AMM2021A01), Postgraduate Research & Practice Innovation Program of Jiangsu Province (No. KYCX20_0091), City University of Hong Kong Strategic Research Grant (SRG) (No. 7005505), as well as City University of Hong Kong Donation Research Grant (DON-RMG No. 9229021).

## References

[1] U. Filipović, R.G. Dahmane, S. Ghannouchi, A. Zore, K. Bohinc, Bacterial adhesion on orthopedic implants, Adv. Colloid Interface 283 (2020), 102228, https://doi.org/10.1016/j.cis.2020.102228.
[2] C. Hu, D. Ashok, D.R. Nisbet, V. Gautam, Bioinspired surface modification of orthopedic implants for bone tissue engineering, Biomaterials 219 (2019), 119366, https://doi.org/10.1016/j.biomaterials. 2019.119366.
[3] J.L. Wang, J.K. Xu, C. Hopkins, D.H.K. Chow, L. Qin, Biodegradable magnesium-based implants in orthopedics – a general review and perspectives, Advanced Science 7 (8) (2020), 1902443, https://doi.org/10.1002/advs.201902443.
[4] Y.F. Zheng, X.N. Gu, F. Witte, Biodegradable metals, Mater. Sci. Eng. R. Rep. 77 (2014) 1–34, https://doi.org/10.1016/j.mser.2014.01.001.
[5] B.D. Ratner, Biomaterials: been there, done that, and evolving into the future, Annu. Rev. Biomed. Eng. 21 (1) (2019) 171–191, https://doi.org/10.1146/annurev-bioeng-062117-120940.
[6] Q. Chen, G.A. Thouas, Metallic implant biomaterials, Mater. Sci. Eng. R. Rep. 87 (2015) 1–57, https://doi.org/10.1016/j.mser.2014.10.001.
[7] Z. Sheikh, S. Najeeb, Z. Khurshid, V. Verma, H. Rashid, M. Glogauer, Biodegradable materials for bone repair and tissue engineering applications, Materials 8 (9) (2015) 5744–5794, https://doi.org/10.3390/ma8095273.
[8] Z. Yin, W. Qi, R. Zeng, X. Chen, C. Gu, S. Guan, Y. Zheng, Advances in coatings on biodegradable magnesium alloys, J. Magnes. Alloys 8 (1) (2020) 42–65, https://doi.org/10.1016/j.jma. 2019.09.008.
[9] H. Hornberger, S. Virtanen, A.R. Boccaccini, Biomedical coatings on magnesium alloys – a review, Acta Biomater. 8 (7) (2012) 2442–2455, https://doi.org/10.1016/j.actbio.2012.04.012.
[10] G. Barati Darband, M. Aliofkhazraei, P. Hamghalam, N. Valizade, Plasma electrolytic oxidation of magnesium and its alloys: mechanism, properties and applications, J. Magnes. Alloys 5 (1) (2017) 74–132, https://doi.org/10.1016/j.jma.2017.02.004.
[11] J.G. Acheson, E.A. Gallagher, J. Ward, S. Mckillop, B. Fitzgibbon, A.R. Boyd, B. J. Meenan, P. Lemoine, J.P. Mcgarry, Shear testing and failure modelling of calcium phosphate coated AZ31 magnesium alloys for orthopaedic applications, Surf. Coat. Technol. 429 (2022), 127944, https://doi.org/10.1016/j.surfcoat.2021.12.
[12] W. Habraken, P. Habibovic, M. Epple, M. Bohner, Calcium phosphates in biomedical applications: materials for the future? Mater. Today 19 (2) (2016) 69–87, https://doi.org/10.1016/j.mattod.2015. 10.008.
[13] K. Lin, C. Wu, J. Chang, Advances in synthesis of calcium phosphate crystals with controlled size and shape, Acta Biomater. 10 (10) (2014) 4071–4102, https://doi.org/10.1016/j.actbio.2014.06.017.
[14] N. Eliaz, N. Metoki, Calcium phosphate bioceramics: a review of their history, structure, properties, coating technologies and biomedical applications, Materials 10 (4) (2017) 334, https://doi.org/10.3390/ma10040334.
[15] M. Sadat-Shojai, M. Khorasani, E. Dinpanah-Khoshdargi, A. Jamshidi, Synthesis methods for nanosized hydroxyapatite with diverse structures, Acta Biomater. 9 (8) (2013) 7591–7621, https://doi.org/10.1016/j.actbio.2013.04.012.
[16] L. Ling, S. Cai, Q. Li, J. Sun, X. Bao, G. Xu, Recent advances in hydrothermal modification of calcium phosphorus coating on magnesium alloy, J. Magnes. Alloys 10 (1) (2022) 62–80, https://doi.org/10.1016/j.jma.2021.05.014.
[17] S. Shen, S. Cai, Y. Li, R. Ling, F. Zhang, G. Xu, F. Wang, Microwave aqueous synthesis of hydroxyapatite bilayer coating on magnesium alloy for orthopedic application, Chem. Eng. J. 309 (2017) 278–287, https://doi.org/10.1016/j.cej.2016.10.043.
[18] Y. Lin, S. Cai, S. Jiang, D. Xie, R. Ling, J. Sun, J. Wei, K. Shen, G. Xu, Enhanced corrosion resistance and bonding strength of mg substituted β-tricalcium phosphate/Mg(OH)2 composite coating on magnesium alloys via one-step hydrothermal method, J. Mech. Behav. Biomed. 90 (2019) 547–555, https://doi.org/10.1016/j.jmbbm.2018.11.007.
[19] W. Cui, E. Beniash, E. Gawalt, Z. Xu, C. Sfeir, Biomimetic coating of magnesium alloy for enhanced corrosion resistance and calcium phosphate deposition, Acta Biomater. 9 (10) (2013) 8650–8659, https://doi.org/10.1016/j.actbio.2013.06.031.
[20] B. Lin, M. Zhong, C. Zheng, L. Cao, D. Wang, L. Wang, J. Liang, B. Cao, Preparation and characterization of dopamine-induced biomimetic hydroxyapatite coatings on the AZ31 magnesium alloy, Surf. Coat. Technol. 281 (2015) 82–88, https://doi.org/10.1016/j.surfcoat.2015.09.033.
[21] P. Liu, J. Wang, X. Yu, X. Chen, S. Li, D. Chen, S. Guan, R. Zeng, L. Cui, Corrosion resistance of bioinspired DNA-induced Ca–P coating on biodegradable magnesium alloy, J. Magnes. Alloys 7 (1) (2019) 144–154, https://doi.org/10.1016/j.jma.2019.01.004.
[22] S. Zhao, F. Caruso, L. Dähne, G. Decher, B.G. De Geest, J. Fan, N. Feliu, Y. Gogotsi, P.T. Hammond, M.C. Hersam, A. Khademhosseini, N. Kotov, S. Leporatti, Y. Li, F. Lisdat, L.M. Liz-Marzán, S. Moya, P. Mulvaney, A.L. Rogach, S. Roy, D. G. Shchukin, A.G. Skirtach, M.M. Stevens, G.B. Sukhorukov, P.S. Weiss, Z. Yue, D. Zhu, W.J. Parak, The future of layer-by-layer assembly: a tribute toacs nano associate editor helmuth möhwald, ACS Nano 13 (6) (2019) 6151–6169, https://doi.org/10.1021/acsnano.9b03326.
[23] J.J. Richardson, M. Bjornmalm, F. Caruso, Multilayer assembly. Technology-driven layer-by-layer assembly of nanofilms, Science 348 (6233) (2015), a2491, https://doi.org/10.1126/science.aaa2491.

[24] X. Zhang, H. Chen, H. Zhang, Layer-by-layer assembly: from conventional to unconventional methods, Chem. Commun. 14 (2007) 1395–1405, https://doi.org/10.1039/B615590A.
[25] D. Alkekhia, P.T. Hammond, A. Shukla, Layer-by-layer biomaterials for drug delivery, Annu. Rev. Biomed. Eng. 22 (1) (2020) 1–24, https://doi.org/10.1146/annurev-bioeng-060418-052350.
[26] M. Hu, H. Chang, H. Zhang, J. Wang, W. Lei, B. Li, K. Ren, J. Ji, Mechanical adaptability of the mmp-responsive film improves the functionality of endothelial cell monolayer, Adv. Healthc. Mater. 6 (14) (2017) 1601410, https://doi.org/10.1002/adhm.201601410.
[27] Y. Zhao, H. Liu, C. Li, Y. Chen, S. Li, R. Zeng, Z. Wang, Corrosion resistance and adhesion strength of a spin-assisted layer-by-layer assembled coating on AZ31 magnesium alloy, Appl. Surf. Sci. 434 (2018) 787–795, https://doi.org/10.1016/j.apsusc.2017.11.012.
[28] L. Cui, S. Cheng, L. Liang, J. Zhang, S. Li, Z. Wang, R. Zeng, In vitro corrosion resistance of layer-by-layer assembled polyacrylic acid multilayers induced Ca–P coating on magnesium alloy AZ31, Bioactive Mater. 5 (1) (2020) 153–163, https://doi.org/10.1016/j.bioactmat.2020.02.001.
[29] W. Jin, G. Wu, H. Feng, W. Wang, X. Zhang, P.K. Chu, Improvement of corrosion resistance and biocompatibility of rare-earth WE43 magnesium alloy by neodymium self-ion implantation, Corros. Sci. 94 (2015) 142–155, https://doi.org/10.1016/j.corsci.2015.01.049.
[30] M. Ezechieli, M. Ettinger, C. König, A. Weizbauer, P. Helmecke, R. Schavan, A. Lucas, H. Windhagen, C. Becher, Biomechanical characteristics of bioabsorbable magnesium-based (mgyrezr-alloy) interference screws with different threads, Knee Surg. Sports Traumatol. Arthrosc. 24 (12) (2016) 3976–3981, https://doi.org/10.1007/s00167-014-3325-6.
[31] L. Zhang, J. Pei, H. Wang, Y. Shi, J. Niu, F. Yuan, H. Huang, H. Zhang, G. Yuan, Facile preparation of poly(lactic acid)/brushite bilayer coating on biodegradable magnesium alloys with multiple functionalities for orthopedic application, Acs Appl. Mater. Inter. 9 (11) (2017) 9437–9448, https://doi.org/10.1021/acsami.7b00209.
[32] M. Müller, The anomalous influence of polyelectrolyte concentration on the deposition and nanostructure of poly(ethyleneimine)/poly(acrylic acid) multilayers, Molecules 24 (11) (2019) 2141, https://doi.org/10.3390/molecules24112141.
[33] H. Wang, C.J. Lin, R. Hu, F. Zhang, L.W. Lin, A novel nano-micro structured octacalcium phosphate/protein composite coating on titanium by using an electrochemically induced deposition, J. Biomed. Mater. Res. A 87 (3) (2008) 698–705, https://doi.org/10.1002/jbm.a.31653.
[34] E. Yılmaz, B. Çakıroğlu, A. Gökçe, F. Findik, H.O. Gulsoy, N. Gulsoy, Ö. Mutlu, M. Özacar, Novel hydroxyapatite/graphene oxide/collagen bioactive composite coating on Ti16NB alloys by electrodeposition, Materials Science and Engineering: C 101 (2019) 292–305, https://doi.org/10.1016/j.msec.2019.03.078.
[35] V. Selin, J.F. Ankner, S.A. Sukhishvili, Nonlinear layer-by-layer films: effects of chain diffusivity on film structure and swelling, Macromolecules 50 (16) (2017) 6192–6201, https://doi.org/10.1021/acs.macromol.7b01218.
[36] S.S. Shiratori, M.F. Rubner, pH-dependent thickness behavior of sequentially adsorbed layers of weak polyelectrolytes, Macromolecules 33 (11) (2000) 4213–4219, https://doi.org/10.1021/ma991645q.
[37] Y. Yang, M. Haile, Y.T. Park, F.A. Malek, J.C. Grunlan, Super gas barrier of all-polymer multilayer thin films, Macromolecules 44 (6) (2011) 1450–1459, https://doi.org/10.1021/ma1026127.
[38] A. Dey, P.H. Bomans, F.A. Muller, J. Will, P.M. Frederik, G. de With, N. A. Sommerdijk, The role of prenucleation clusters in surface-induced calcium phosphate crystallization, Nat. Mater. 9 (12) (2010) 1010–1014, https://doi.org/10.1038/nmat2900.
[39] H. Jiang, X. Liu, G. Zhang, Y. Li, Kinetics and template nucleation of self-assembled hydroxyapatite nanocrystallites by chondroitin sulfate, J. Biol. Chem. 280 (51) (2005) 42061–42066, https://doi.org/10.1074/jbc.M412280200.
[40] Y. Qi, Z. Ye, A. Fok, B.N. Holmes, M. Espanol, M. Ginebra, C. Aparicio, Effects of molecular weight and concentration of poly(acrylic acid) on biomimetic mineralization of collagen, ACS Biomater Sci. Eng. 4 (8) (2018) 2758–2766, https://doi.org/10.1021/acsbiomaterials. 8b00512.
[41] J. Sharma, K. Tewari, R.K. Arya, Diffusion in polymeric systems–a review on free volume theory, Prog. Org. Coat. 111 (2017) 83–92, https://doi.org/10.1016/j.porgcoat.2017.05.004.
[42] G. Liu, Z. Jiang, C. Chen, L. Hou, B. Gao, H. Yang, H. Wu, F. Pan, P. Zhang, X. Cao, Preparation of ultrathin, robust membranes through reactive layer-by-layer (lbl) assembly for pervaporation dehydration, J. Membrane Sci. 537 (2017) 229–238, https://doi.org/10.1016/j.memsci.2017.05.025.
[43] Y. Gu, J. Zhao, J.A. Johnson, Polymernetzwerke: von kunststoffen und gelen zu porösen gerüsten, Angew. Chem. 132 (13) (2020) 5054–5085, https://doi.org/10.1002/ange.201902900.
[44] G. Liu, Z. Jiang, X. Cheng, C. Chen, H. Yang, H. Wu, F. Pan, P. Zhang, X. Cao, Elevating the selectivity of layer-by-layer membranes by in situ bioinspired mineralization, J. Membrane Sci. 520 (2016) 364–373, https://doi.org/10.1016/j.memsci.2016.07.056.
[45] L. Fathyunes, J. Khalil-Allafi, M. Moosavifar, Development of graphene oxide/calcium phosphate coating by pulse electrodeposition on anodized titanium: biocorrosion and mechanical behavior, J. Mech. Behav. Biomed. 90 (2019) 575–586, https://doi.org/10.1016/j.jmbbm.2018.11.011.
[46] A.J. Hill, A.W. Thornton, R.H.J. Hannink, J.D. Moon, B.D. Freeman, Role of free volume in molecular mobility and performance of glassy polymers for corrosion-protective coatings, Corros. Eng. Sci. Technol. 55 (2) (2020) 145–158, https://doi.org/10.1080/1478422X. 2019.1701237.
[47] S. Heinz, J. Tu, M. Jackson, J. Wiggins, Digital image correlation analysis of strain recovery in glassy polymer network isomers, Polymer 82 (2016) 87–92, https://doi.org/10.1016/j.polymer. 2015.11.026.
[48] J. Faugier-Tovar, F. Lazar, C. Marichy, C. Brylinski, Influence of the lattice mismatch on the atomic ordering of ZnO grown by atomic layer deposition onto single crystal surfaces with variable mismatch (inp, gaas, gan, sic), Condens. Matter 2 (1) (2017) 3, https://doi.org/10.3390/condmat2010003.
[49] P.A. Gabrys, S.E. Seo, M.X. Wang, E. Oh, R.J. Macfarlane, C.A. Mirkin, Lattice mismatch in crystalline nanoparticle thin films, Nano Lett. 18 (1) (2018) 579–585, https://doi.org/10.1021/acs.nanolett.7b04737.